Thermal transformation of δ-MnO₂ nanoflowers studied by *in-situ* TEM

SUN YuGang[1*], LIU YuZi[1], TRUONG Tu T.[1] & REN Yang[2]

[1]*Center for Nanoscale Materials, Argonne National Laboratory, 9700 South Cass Avenue, Argonne, Illinois 60439, US*
[2]*X-Ray Science Division, Argonne National Laboratory, 9700 South Cass Avenue, Argonne, Illinois 60439, US*

In-situ transmission electron microscopy in combination with a heating stage has been employed to real-time monitor variations of δ-phase MnO_2 nanoflowers in terms of their morphology and crystalline structures upon thermal annealing at elevated temperatures up to ~665 °C. High-temperature annealing drives the diffusion of the small δ-MnO_2 nanocrystallites within short distances less than 15 nm and the fusion of the adjacent δ-MnO_2 nanocrystallites, leading to the formation of larger crystalline domains including highly crystalline nanorods. The annealed nanoflowers remain their overall flower-like morphology while they are converted to α-MnO_2. The preferred transformation of the δ-MnO_2 to the α-MnO_2 can be ascribed to the close lattice spacing of most crystalline lattices between δ-MnO_2 and α-MnO_2, that might lead to a possible epitaxial growth of α-MnO_2 lattices on the δ-MnO_2 lattices during the thermal annealing process.

δ-MnO₂ nanoflowers, α-MnO₂, thermal annealing, *in-situ* TEM, mechanism study

1   Introduction

Manganese dioxide (MnO_2) and derivatives represent a class of benchmark electrode materials for electrochemical energy storage devices including supercapacitors [1, 2], lithium-ion batteries [3, 4], and lithium-air batteries [5, 6]. For example, MnO_2 nanostructures have been integrated into the porous oxygen cathodes in lithium-air batteries to catalyze the oxygen reduction reactions associated with the formation of lithium oxides/lithium peroxides and the oxygen evolution reactions associated with the dissociation of lithium oxides/ lithium peroxides [5]. Their catalytic performance has been revealed to strongly rely on the morphology and crystalline phase of the MnO_2 nanoparticles. Comparison of different manganese oxide materials shows that the cathodes containing α-MnO_2 nanowires exhibit the best performance with discharge capacity that is at least two times higher than cathodes made of other forms of manganese oxide (e.g., α-MnO_2 bulk material and β-MnO_2 nanowires). In general, MnO_2 nanoparticles exhibit a large variety of crystallographic structures (e.g., α, β, δ, γ, and λ forms). Lattices with different crystalline structures exhibit tunnels or interlayers with gaps of different magnitudes because the repeated MnO_6 octahedron units in MnO_2 share their faces and edges in different ways [7]. This structural diversity of MnO_2 results in significant challenges when trying to optimize the correlation between the crystallographic structures of MnO_2 nanoparticles and device performance. As a result, synthesis of MnO_2 nanoparticles with a single high-purity crystallographic phase is important and challenging due to their high sensitivity towards reaction conditions. For example, many methods including co-precipitation [8], sol-gel techniques [9], hydrothermal/solvothermal redox reactions [10], high viscosity processes [11], solution combustion [12], etc. have been studied for the synthesis of crystalline MnO_2 nanoparticles. The resulting nanoparticles exhibit varying morphologies (e.g., plates, urchin-like architectures,

*Corresponding author (email: ygsun@anl.gov)

flowers, cubes, wires, rods, belts, hollow spheres, etc.) and crystallographic phases, which are two inter-dependent parameters of the MnO_2 nanoparticles. However, the dependence of MnO_2 nanoparticles on reaction conditions and the growth mechanism are still not well understood. For instance, Munichandraiah and co-workers found that thermal annealing of nearly X-ray amorphous MnO_2 nanoparticles synthesized at room temperatures could transform them to highly crystalline α-MnO_2 nanorods [13]. The detailed transformation in terms of morphology and crystallinity involved in the thermal annealing process has not been studied yet. In this work, we report the use of *in-situ* transmission electron microscopy (TEM) for real-time monitoring the nanophase evolution of δ-MnO_2 nanoflowers under thermal annealing in high vacuum TEM environment.

2 Experimental

2.1 Synthesis of δ-MnO_2 nanoflowers

The δ-MnO_2 nanoflowers were synthesized through a microwave-assistant hydrothermal process in which an aqueous solution containing both potassium permanganate ($KMnO_4$) and hydrochloric acid (HCl) in a sealed glass-tube reactor was heated by microwave radiation in a CEM® Discover system. In a typical synthesis, 0.33×10^{-3} molar of $KMnO_4$ (Sigma-Aldrich) and 1 mL of 1.2 M HCl solution (Sigma-Aldrich) were added to 5 mL of deionized water. The mixture was then sealed in a 10-mL glass-tube reactor. Placing the reactor in the microwave system enabled heating the solution to 150 °C within ~1 min. Continuously heating the solution for an additional 5 min at 150 °C led to a completion of the redox reaction between $KMnO_4$ and HCl, resulting in the formation of δ-MnO_2 nanoflowers. The reaction solution was then quickly cooled down to room temperature with an assistance of nitrogen blow. The resulting black dispersion was centrifuged, washed with deionized water, and dried in an oven set at 60 °C in air.

2.2 TEM characterization

A heating sample holder from Gatan was employed to carry out the *in-situ* heating experiment on a Tecnai F20 transmission electron microscope operated at a voltage of 200 kV. The as-synthesized δ-MnO_2 nanoflowers were first dispersed in ethanol with an assistance of ultrasonication. Placing a small drop of this dispersion on a gold TEM grid coated with an ultrathin carbon film followed by evaporating ethanol finished the preparation of a sample for TEM characterization. The sample temperature was controlled by manually adjusting the heating current through the external controller. Once the temperature

reached the set value and stabilized for 3 min, selected-area electron diffraction (SAED) patterns and bright-field TEM images were recorded. In order to acquire high-quality high-resolution TEM (HRTEM) images, the annealed grid was transferred to a regular double-tilt holder to avoid sample drifting.

3 Results and discussion

Reduction of $KMnO_4$ with HCl has been used to synthesize different MnO_2 nanostructures under varying reaction conditions [14]. In general, mixing an aqueous solution of $KMnO_4$ with an aqueous solution of HCl at room temperature cannot immediately induce the thermodynamically favorable redox reaction:

$$2KMnO_4 + 8HCl \rightarrow 2MnO_2 + 3Cl_2 + 2KCl + 4H_2O$$

The reaction rate can be dramatically increased to form solid MnO_2 nanoparticles from the homogeneous aqueous solution once the reaction temperature is elevated. In this work, we applied microwave energy to quickly heat an aqueous solution containing both $KMnO_4$ (0.055 M) and HCl (0.2 M) up to 150 °C in a sealed microwave reactor. It took ~1 min to reach 150 °C at which the reaction lasted 5 min. After the reaction solution was cooled down to room temperature, a black dispersion was formed. The black powders are characterized as quasi-spherical flowers made of interconnected nanosheets (Figure 1(a)). The sizes of the flowers are in the range of 1–2 μm. TEM images of the flowers clearly show that the nanosheets exhibit thicknesses of 2–10 nm. Such small thicknesses make the nanosheets to be mechanically flexible and to be easily folded (Figure 1(b)). HRTEM images reveal that each nanosheet is an assembly of many crystalline domains with sizes less than 5 nm (Figure 1(c)). X-ray diffraction (XRD) pattern of the flowers exhibit reflection peaks that are consistent with the δ-phase of MnO_2 (red curve, Figure 1(d)). The (001) and (002) peaks are intense and symmetric, corresponding to the layered structure of the δ-type MnO_2. The other two peaks at higher angles are asymmetric and are indexed as (−111) and (020) reflections of the δ-type MnO_2 according to the positions of the peak maxima. The broadening and diffusive features of the peaks indicate the small sizes of crystalline domains in the MnO_2 nanoflowers. The lattice fringes observed in the HRTEM image shown in Figure 1(c) exhibit lattice spacing around 2.4 Å that is close to the lattice spacing of the (−111) planes regardless of the orientations of the crystalline domains. Lattice fringes with larger spacing corresponding to the (001) and (002) planes are not observed in the HRTEM image, indicating that the crystalline (001) direction might be perpendicular to the basal surfaces of the nanosheets. The lattice spacing (i.e., 1.425 Å) corresponding to the (020) planes is too small to be observed with the current TEM microscope.
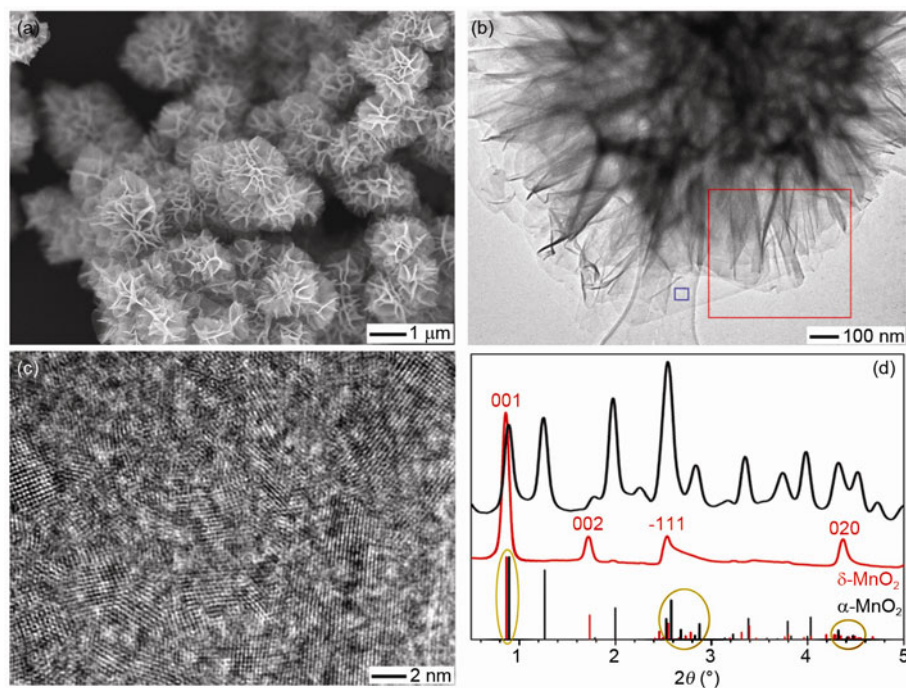
Figure 1 Characterization of the as-synthesized δ-MnO$_2$ nanoflowers. (a) Scanning electron microscopy (SEM) image of a number of nanoflowers. (b) TEM image of an individual nanoflower. (c) HRTEM image of a small portion of a nanosheet highlighted in the blue box in (b). (d) XRD patterns of the nanoflowers (red curve) and the products formed after thermal annealing (black curve) recorded at a synchrotron X-ray beam line with an X-ray beam wavelength of 0.10798 Å. The sticks correspond to the peak position and relative intensity of the standard powder XRD of the δ-MnO$_2$ (red sticks) and the α-MnO$_2$ (black sticks).

The δ-MnO$_2$ flowers consisting of small crystalline domains are not stable at high temperatures. We used *in-situ* heating TEM to real-time monitor the morphological and crystalline transitions of the nanoflowers when the sample is thermally annealed in the vacuum environment. Once the δ-MnO$_2$ flowers are heated, their volume gradually shrinks as the temperature continuously increases. As highlighted in the red box of Figure 1(b), several nanosheets lie on the carbon film of a TEM grid against their flat surfaces. Due to the thin thickness and mechanical flexibility of these nanosheets, they can partially curve and fold to form thick strips that show darker contrast in the TEM image. It is clear that each nanosheet is smooth and continuous before it is heated. Figure 2 presents a series of TEM images of the nanosheets at different temperatures. As indicated by the relative positions of the red arrows in the left-column frames in Figure 2, the shrinkage of the nanosheets can be clearly identified as the temperature gradually increases. When the temperature is high enough (>350 °C), large crystalline domains (i.e., the dots with darker contrast in comparison with the surrounding nanosheets) start to appear, indicating that the small δ-MnO$_2$ domains shown in Figure 1(c) coalesce into large domains. Meanwhile, the widths of folded strips also shrink and these strips separated from their mother nanosheets, resulting in the formation of nanorods at temperatures higher than 550 °C. The volume shrinkage associated with thermal annealing is not reversi-

ble, i.e., the nanorods and large crystalline domains cannot return to the original nanosheets (see the right bottom frame of Figure 2) even after the temperature decreases to room temperature.

The nanostructures formed after thermal annealing followed by cooling down have been characterized with TEM and electron diffraction (ED). As shown in Figure S1, the annealed nanoflower becomes smaller in volume and denser in mass compared with the original flower before annealing (Figure 1(b)). There are many individual nanorods formed in the annealed flower (Figure S1). These nanorods can be clearly identified from the high-magnification TEM images (Figure 3(a)). Closer observation with HRTEM images reveals that each nanorod is highly crystallized and has a continuous crystalline lattice, indicating that individual crystalline domains in the annealed flowers are much larger than the individual crystalline δ-MnO$_2$ domains shown in Figure 1(c). Adjacent to the nanorods there are areas absent of crystalline materials. These observations indicate that the small crystalline δ-MnO$_2$ domains can diffuse and fuse into larger crystalline domains at high temperatures. As highlighted by the blue curves in Figures 3(b) and (c), δ-MnO$_2$ nanocrystallites can only diffuse within limited distances (<15 nm). Such short diffusion length is ascribed to the low mobility of MnO$_2$ in dry solid powders. The diffusion process can be accelerated through heating the δ-MnO$_2$ flowers in aqueous solutions, leading to the formation of nanorods
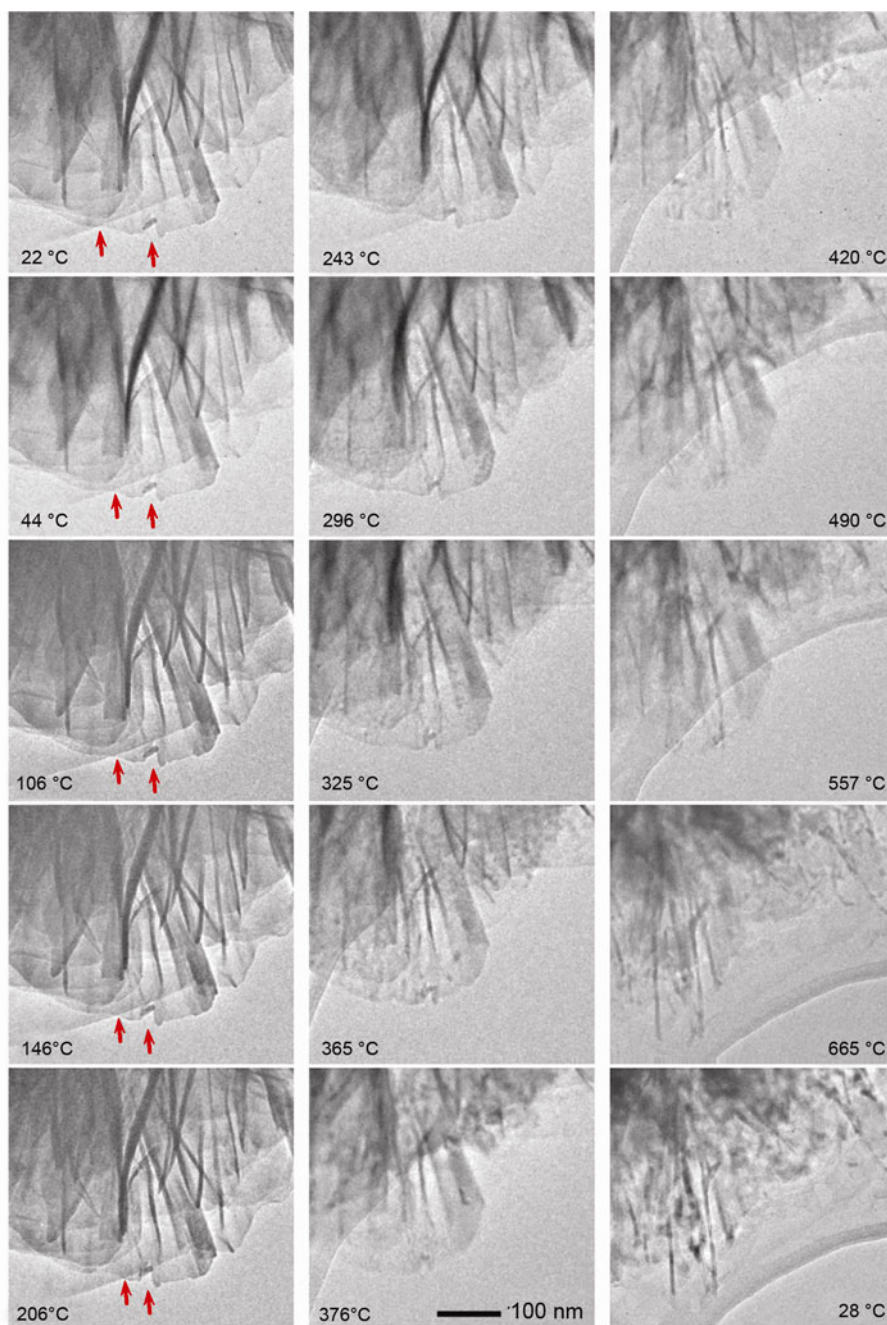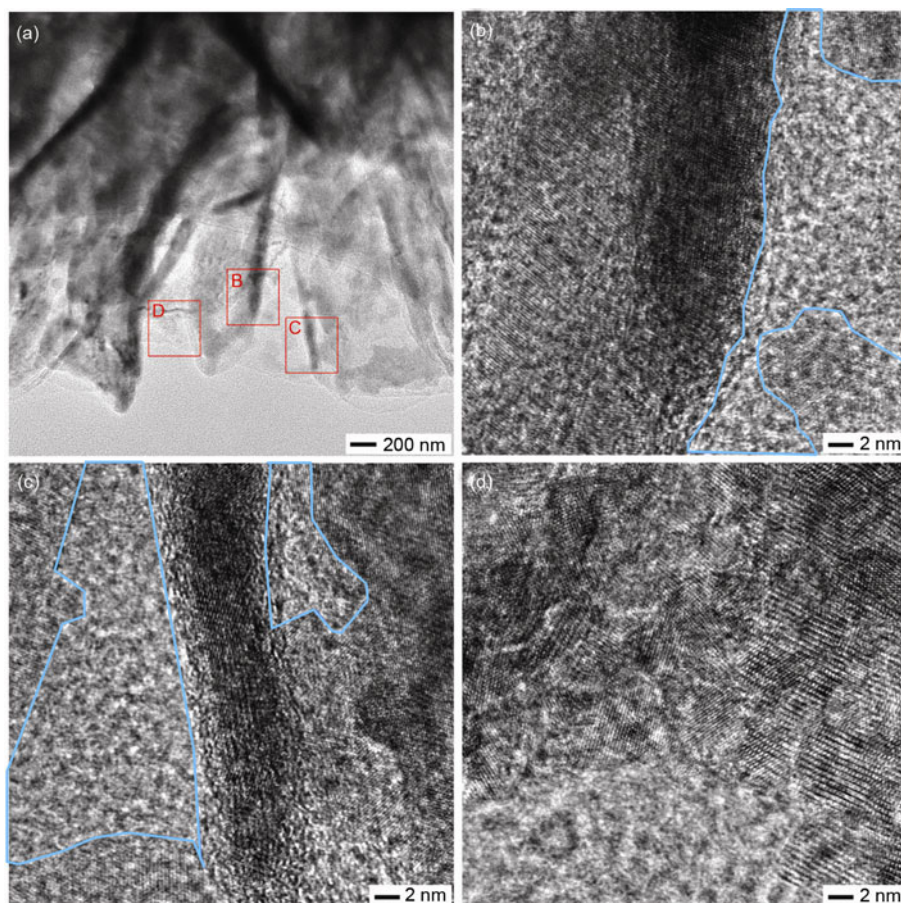
Figure 2   A series of TEM images of the MnO_2 nanosheets recorded at different temperatures. The nanosheets were a portion of a nanoflower highlighted in the red box in Figure 1(b). The temperature shown in each frame was the temperature at which the image was taken. The scale bar applies to all images.

with much larger dimensions [15]. In addition to the transformation of the folded nanosheets into highly crystalline nanorods, the crystalline domains in the flat regions of the nanosheets are also fused to increase the sizes of individual domains (Figure 3(d)).

Lattice fringes in the HRTEM image shown in Figure 3(d) exhibit variations of lattice spacing although all the fringes shown in Figure 1(c) have essentially the same lattice spacing. This difference indicates that thermal annealing drives a crystalline phase transition of the δ-MnO_2 nanoflowers.

Selected-area electron diffraction (SAED) pattern of the area shown in Figure 3(a) indicates the δ-MnO_2 has been converted to α-MnO_2 after thermal annealing at 665 °C (Figure S2). The XRD pattern (black curve, Figure 1(d)) of the annealed product is also consistent with the standard powder diffraction of α-MnO_2 (black sticks, Figure 1(d)). The SAED patterns of the area shown in Figure 2 at different temperatures are presented in Figure 4. The SAED pattern of the nanosheets exhibits only two diffraction rings corresponding to the (−111) and (020) reflections of

Figure 3 Characterization of the MnO_2 nanostructure formed after thermal annealing. (a) TEM image of a portion of a thermally annealed nanoflower highlighted in the red box in Figure S1. (b, c, d) HRTEM images of the areas highlighted in the red boxes in (a) with the corresponding letters. The areas highlighted by the blue curves in (b, c) are absent of crystalline materials.

δ-MnO_2 before they are heated. The absence of (001) and (002) reflections (that are related to the layered structure of the δ-MnO_2 nanodomains) in the SAED pattern is ascribed to that the preferred lamination of the nanosheets on the TEM grid against the basal (001) surfaces of the nanosheets. As the temperature increases, the (−111) diffraction ring of the δ-MnO_2 starts to slightly diffuse at ~206 °C and transforms into two well-separated rings that correspond to the (211)/(121) and (301) reflections of α-MnO_2, respectively, at ~325 °C. Meanwhile, the (020) diffraction ring of δ-MnO_2 is transformed to a diffraction ring that corresponds to the (002) reflection of α-MnO_2. These new diffraction rings of the α-MnO_2 are more intense than those of the δ-MnO_2 shown in the top left frame in Figure 4. Some bright, scattering spots can be observed in the diffraction rings of the α-MnO_2, indicating the formation of large crystalline domains that can scatter the electron beam along certain particular directions. In addition to these three major diffraction rings, many weak diffraction rings with smaller *d* spacing are also observed for the thermally annealed sample and they are consistent with the α-MnO_2.

The evolution of SAED patterns shown in Figure 4 indicates that there might be an epitaxial relationship between the original δ-MnO_2 nanocrystallites and the resulting α-MnO_2 nanodomains during thermal annealing. Such epitaxial correlation is consistent with the fact that most of the α-MnO_2 lattices exhibit similar *d* spacing to the δ-MnO_2 lattices (as highlighted by the yellow ovals in Figure 1(d)).

In summary, the δ-MnO_2 flowers consisting of assembly of nanosheets with thickness of 2–10 nm can be converted to α-MnO_2 flowers through thermal annealing. The thermal annealing process has been studied with *in-situ* TEM by heating the δ-MnO_2 flowers up to 665 °C. Real-time observations of the morphological and structural transitions of the MnO_2 flowers reveal: (1) the small δ-MnO_2 nanocrystalline domains can diffuse to fuse together into larger α-MnO_2 domains including nanorods; (2) the diffusion length of the nanodomains is less than 15 nm, leading to that the flower morphology remains after thermal annealing; (3) lattice spacing of many lattices of the δ-MnO_2 are similar to those of the α-MnO_2, indicating a possible epitaxial relationship exists between the original δ-MnO_2 nanocrystallites and the
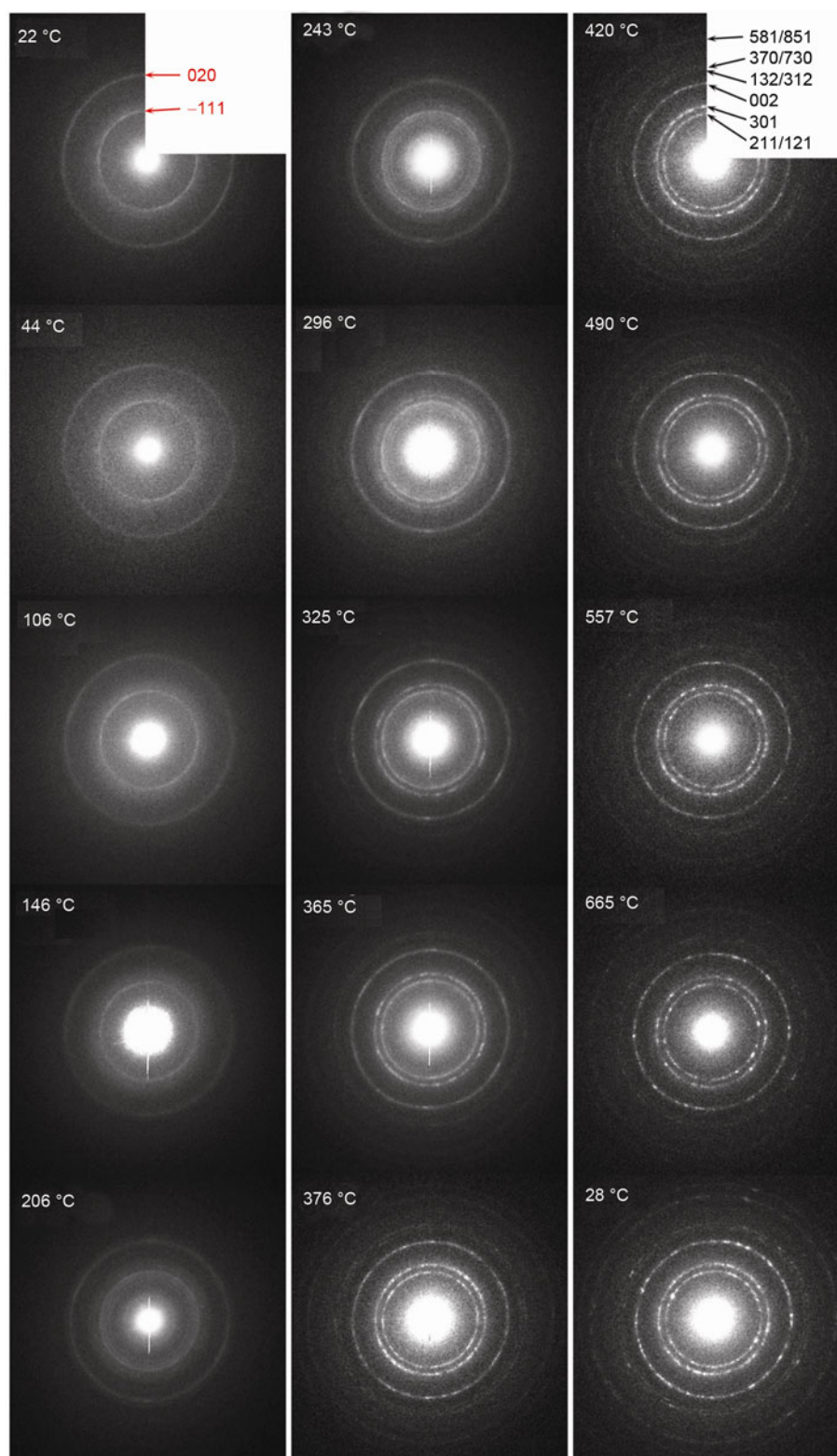
Figure 4 A series of SAED patterns of the MnO_2 nanosheets recorded at different temperatures. The nanosheets were a portion of a nanoflower highlighted in the red box in Figure 1(b). The temperature shown in each frame was the temperature at which the image was taken. The Miller indices in the SAED pattern recorded at 22 °C correspond to the δ-MnO_2 and the Miller indices in the SAED pattern recorded at 420 °C correspond to the α-MnO_2.

resulting α-MnO_2 nanodomains during thermal annealing. Such epitaxial relationship might be responsible for the thermal conversion of the δ-MnO_2 nanoflowers to the flowers made of α-MnO_2 rather than other crystalline phases.

1   Wei W, Cui X, Chen W, Ivey DG. Manganese oxide-based materials as electrochemical supercapacitor electrodes. *Chem Soc Rev*, 2011, 40: 1697–1721

2   Lang X, Hirata A, Fujita T, Chen M. Nanoporous metal/oxide hybrid electrodes for electrochemical supercapacitors. *Nat Nanotechnol*, 2011, 6: 232–236

3   Thackeray MM. Manganese oxides for lithium batteries. *Prog Solid St Chem*, 1997, 25: 1–71

4   Thackeray MM, David WIF, Bruce PG, Goodenough JB. Lithium insertion into manganese spinels. *Mater Res Bull*, 1983, 18: 461–472

5   Débart A, Paterson AJ, Bao J, Bruce PG. α-MnO$_2$ nanowires: A catalyst for the O$_2$ electrode in rechargeable lithium batteries. *Angew Chem Int Ed*, 2008, 47: 4521–4524

6   Bruce PG, Freunberger SA, Hardwick LJ, Tarascon JM. Li-O$_2$ and Li-S batteries with high energy storage. *Nat Mater*, 2012, 11: 19–29

7   Devaraj S, Munichandraiah N. Effect of crystallographic structure of MnO$_2$ on its electrochemical capacitance properties. *J Phys Chem C*, 2008, 112: 4406–4417

8   Brousse T, Toupin M, Dugas R, Athouel L, Crosnier O, Belanger D. Crystalline MnO$_2$ as possible alternatives to amorphous compounds in electrochemical supercapacitors. *J Electrochem Soc*, 2006, 153: A2171–A2180

9   Wang X, Yuan A, Wang Y. Supercapacitive behaviors and their temperature dependence of sol-gel synthesized nanostructured manganese dioxide in lithium hydroxide electrolyte. *J Power Sources*, 2007, 172: 1007–1011

10 Gao T, Fjellvag H, Norby P. Structural and morphological evolution of beta-MnO$_2$ nanorods during hydrothermal synthesis. *Nanotechnology*, 2009, 20: 055610(7)

11 Ye C, Lin ZM, Hui SZ. Electrochemical and capacitance properties of rod-shaped MnO$_2$ for supercapacitor. *J Electrochem Soc*, 2005, 152: A1272–A1278

12 Yu P, Zhang X, Chen Y, Ma Y. Solution-combustion synthesis of ε-MnO$_2$ for supercapacitors. *Mater Lett*, 2010, 64: 61–64

13 Ragupathy P, Park DH, Campet G, Vasan HN, Hwang SJ, Choy JH, Munichandraiah N. Remarkable capacity retention of nanostructured manganese oxide upon cycling as an electrode material for supercapacitor. *J Phys Chem C*, 2009, 113: 6303–6309

14 Zhou M, Zhang X, Wei J, Zhao S, Wang L, Feng B. Morphology-controlled synthesis and novel microwave absorption properties of hollow urchinlike α-MnO$_2$ nanostructures. *J Phys Chem C*, 2011, 115: 1398–1402

15 Xu M, Kong L, Zhou W, Li H. Hydrothermal synthesis and pseudocapacitance properties of α-MnO$_2$ hollow spheres and hollow urchins. *J Phys Chem C*, 2007, 111: 19141–19147